

# The Population of Dark Matter Subhaloes: Mass Functions and Average Mass Loss Rates

Carlo Giocoli<sup>1</sup>, Giuseppe Tormen<sup>1</sup> & Frank C. van den Bosch<sup>2</sup> \*

<sup>1</sup>*Dipartimento di Astronomia, Università degli Studi di Padova, Vicolo dell'osservatorio 2 I-35122 Padova, Italy*

<sup>2</sup>*Max-Planck-Institute for Astronomy, Königstuhl 17, 69117 Heidelberg, Germany*

## ABSTRACT

Using a cosmological N-Body simulation and a sample of re-simulated cluster-like haloes, we study the mass loss rates of dark matter subhaloes, and interpret the mass function of subhaloes at redshift zero in terms of the evolution of the mass function of systems accreted by the main halo progenitor (hereafter called the ‘unevolved subhalo mass function’). When expressed in terms of the ratio between the mass of the subhalo at the time of accretion,  $m_v$ , and the present day host mass,  $M_0$ , the unevolved subhalo mass function is found to be universal, in that it is independent of the mass of the host halo. However, the subhalo mass function at redshift zero (hereafter called the ‘evolved subhalo mass function’) clearly depends on  $M_0$ , in that more massive host haloes host more subhaloes. In order to relate the unevolved and evolved subhalo mass functions, we measure the subhalo mass loss rate as a function of host mass and redshift. We find that the average, specific mass loss rate of dark matter subhaloes depends mainly on redshift, with only a very weak dependence on the instantaneous ratio between the mass of the subhalo,  $m_{sb}$ , and that of the host halo at that time  $M_v$ . In fact, to good approximation, subhalo masses ‘decay’ exponentially, with a decay-time that is proportional to the instantaneous dynamical time of the host halo. Combined with the fact that more massive haloes assemble later, these results suggest a pleasingly simple picture for the evolution and mass dependence of the evolved subhalo mass function. Less massive host haloes accrete their subhaloes earlier, which are thus subjected to mass loss for a longer time. In addition, their subhaloes are typically accreted by denser hosts, which causes an additional boost of the mass loss rate. To test the self-consistency of this picture, we use semi-analytical merger trees constructed using the extended Press-Schechter formalism, and evolve the subhalo populations using the average mass loss rates obtained from our simulations. The resulting subhalo mass functions are found to be in good agreement with the simulations. Our model can be applied to semi-analytical methods of galaxy formation, to accurately follow the time evolution of subhalo masses.

**Key words:** galaxies: halo - cosmology: theory - dark matter - methods: numerical simulations - galaxies: interactions

## 1 INTRODUCTION

Understanding structure formation is a fundamental topic in modern cosmology. In the current  $\Lambda$ CDM concordance cosmology, the matter density of the Universe is dominated by cold dark matter (CDM), whose gravitational evolution gives rise to a population of virialized dark matter haloes spanning a wide range of masses. Numerical simulations of

structure formation in a CDM universe predict that these dark matter haloes contain a population of subhaloes, which are the remnants of halos accreted by the host, and which are eroded by the combined effects of gravitational heating and tidal stripping in the potential well of the main halo.

Understanding the evolution of the subhalo mass function, as function of cosmology, redshift, and host halo mass, is of paramount importance, with numerous applications. For one, subhaloes are believed to host satellite galaxies, which can thus be used as luminous tracers of the subhalo population. In particular, linking the observed abundances

\* E-mail: carlo.giocoli@unipd.it, giuseppe.tormen@unipd.it, vdbosch@mpia-hd.mpg.de.

of satellite galaxies to the expected abundance of subhaloes, provides useful insights into the physics of galaxy formation (e.g., Moore et al. 1999; Bullock et al. 2000; Somerville 2002; Kravtsov et al. 2006; Vale & Ostriker 2006). Studies along these lines indicate that galaxy formation becomes extremely inefficient in low mass haloes, and suggest that there may well be a large population of low mass subhaloes with no optical counterpart (e.g., Moore et al. 1999; Stoehr et al. 2002; Kravtsov et al. 2004). In principle, though, these truly ‘dark’ subhaloes may potentially be detected via  $\gamma$ -ray emission due to dark matter annihilation in their central cores (Stoehr et al. 2003; Bertone 2006; Pieri et al. 2007; Diemand et al. 2007), or via their impact on the flux-ratio statistics of multiply-lensed quasars (e.g., Metcalf & Madau 2001; Dalal & Kochanek 2002). Alternatively, these techniques may be used to constrain the abundance of subhaloes, which in turn has implications for cosmological parameters and/or the nature of dark matter. The evolution of the subhalo mass function is also of importance for the survival probability of disk galaxies (e.g., Toth & Ostriker 1992; Benson et al. 2004; Steward et al. 2007) and even has implications for direct detection experiments of dark matter (e.g., Goerdt et al. 2007). Finally, understanding the rate at which dark matter subhaloes loose mass has important implications for their dynamical friction times, and thus for the merger rates of galaxies (e.g., Benson et al. 2002; Zentner & Bullock 2003; Taylor & Babul 2004).

Despite significant progress in the last years, there are still numerous issues that are insufficiently understood. What is the mass function of haloes accreted onto the main progenitor of a present day host halo? How do the orbits and masses of subhaloes evolve as they are subjected to dynamical friction, tidal forces and close encounters with other subhaloes? How does this depend on the properties of the host halo? In this paper we address these questions using high-resolution numerical simulations. We trace back the evolution of self-bound substructures identified in present-day host haloes up to the point where they are first accreted by the main progenitor of the host halo. Using this method we are able to link the present-day population of subhaloes to the merging history of the host system. We will show that larger systems, forming at lower redshifts and so accreting their satellites more recently, contain at the end more subhaloes than smaller hosts (see also Gao et al. 2004; van den Bosch et al. 2005).

In Section 2 we describe the simulations used. In Section 2.3 we present the algorithms employed to identify the haloes and to follow their merging history trees. In Section 3 we show how the unevolved subhalo mass function is constructed from the merger tree of present-day halos and suggest an analytical fit. In Section 4 we explain how subhaloes are identified at the present time. In Section 5 we calculate the mass loss rate for subhaloes, and characterize its dependence on host halo mass and on redshift. In Section 6 we present Monte Carlo simulations that reproduce the subhalo mass function measured in the  $N$ -body simulations. Finally, in Section 7 we summarize our results and draw some conclusions.

## 2 THE SIMULATIONS

To study the evolution of the subhalo population of dark matter haloes we use two different types of simulations: a set of 48 massive haloes that have been extracted from a large cosmological simulation and resimulated at much higher resolution, and a set of two large, cosmological simulations that probe a much larger dynamic range in host halo masses.

### 2.1 Resimulations

Our sample of 48 resimulated dark matter haloes is extracted from ten high-resolution  $N$ -body resimulations of galaxy clusters, containing  $512^3$  particles in a cube  $479 \text{ Mpc}/h$  on a side. All simulations assume a flat  $\Lambda$ CDM model with  $\Omega_0 = 0.3$ ,  $h = 0.7$ ,  $\sigma_8 = 0.9$  and  $\Omega_b = 0.04$  (Yoshida, Sheth & Diaferio 2001). The masses of the haloes selected to be resimulated cover the range  $5.1 \times 10^{13} - 2.3 \times 10^{15} M_\odot/h$  at redshift  $z = 0$ .

For the resimulations, we adopt a particle mass of  $1.3 \times 10^9 M_\odot/h$  and a gravitational softening length of  $\epsilon = 5 \text{ kpc}/h$  (Plummer equivalent). The initial conditions for the resimulation are generated with higher mass and force resolution using the Zoomed Initial Condition technique (ZIC, Tormen et al. 1997): halo Lagrangian regions are populated with a larger number of less massive particles, and additional small-scale power is added appropriately. The new initial conditions are evolved using the Tree-SPH code Gadget2 (Springel 2005) from redshift  $z = 60$  to the present time, using dark matter particles only. We study these resimulations using 88 output times equally spaced between  $z = 10$  and  $z = 0$ . Figure 1 shows an example of one of these resimulated cluster-sized haloes, embedded in its surrounding large-scale structure. The cluster is resolved with more than one million particles within its virial radius, and there are roughly  $6 \times 10^6$  high resolution dark matter particles inside  $20 \text{ Mpc}/h$ . See Dolag et al. (2005) for further details.

### 2.2 Cosmological N-Body Simulations

We will also make use of two cosmological  $N$ -body simulations. The first is the so called ‘‘GIF2’’ simulation (Gao et al. 2004), a periodic cube of side  $110 \text{ Mpc}/h$  assuming the concordance  $\Lambda$ CDM model ( $\Omega_\Lambda, \Omega_b h^2, h, \sigma_8$ ) = (0.7, 0.0196, 0.7, 0.9). The index of the initial power spectrum as be chosen  $n = 1$ , with the transfer function produced by CMBFAST (Seljak & Zaldarriaga 1996). GIF2 contains  $400^3$  dark matter particles, each of mass  $1.73 \times 10^9 M_\odot/h$ . We will use 50 output times logarithmically spaced between  $z = 10$  and  $z = 0$ , which suffices to construct accurate halo and subhalo merging history trees using the method of Tormen et al. (2004). The numerical data of the GIF2 simulation are publicly available at <http://www.mpa-garching.mpg.de/Virgo>.

Finally, as a consistency check, part of the analysis done on GIF2 was repeated on the lower resolution GIF box ( $\Lambda$ CDM each of mass  $1.4 \times 10^{10} M_\odot/h$ ), which has the same cosmological parameters of the GIF2 simulation. See Kauffmann et al. (1999) for a detailed description of this simulation.



**Figure 1.** A cluster of the resimulated sample resolved with  $2 \times 10^6$  particles within the virial radius and  $6 \times 10^6$  high resolution particles within 40 Mpc/h.

Sim. name	11.5-12	12-12.5	12.5-13	13-13.5	13.5-14	14-14.5	> 14.5
Resimulations	-	-	-	-	21	17	10
GIF	-	-	2693	971	290	99	16
GIF2	8305	3349	1186	461	127	35	4

**Table 1.** The number of haloes in each logarithmic mass bin for the different simulations. For GIF & GIF2 we consider all haloes with a least more than 200 particles within their virial radius at redshift zero and whose main progenitor never has a virial mass exceeding the final value by more than ten percent. For the resimulated haloes we follow the merger tree and the satellites populations for all the haloes with more than 40000 particles at the present time.

### 2.3 Halo-Finder & Merger History Tree

We adopt the spherical overdensity criterion to identify haloes at each simulation output time (also called ”snapshot”). For each snapshot we estimate the local dark matter density at the position of each particle by calculating the

distance to the tenth closest neighbor. We assign to each particle a local density  $\rho_{i,\text{DM}} \propto d_{i,10}^{-3}$ , sort particles in density and take as centre of the first halo the position of the densest particle. We then grow a sphere of matter around this centre, and stop when the mean density within the sphere

falls below the virial value appropriate for the cosmological model at that redshift; for the definition of virial density we adopted the model of Eke et al. (1996); for example, at redshift  $z = 0$  the virial density is  $\rho_v = 324\rho_b$ , with  $\rho_b$  the mean background density of the universe.

At this point we assign all particles within the sphere to the newly formed halo, and remove them from the global list. We take the centre of the next halo at the position of the densest particle among the remaining ones, and grow a second sphere. We continue in this manner until all particles are screened. We include in our catalogue only haloes with at least 10 particles within the virial radius; particles not ending up in any halo are considered as "field" or "dust" particles.

We then build the merging history tree for all haloes in the simulation (or resimulation) using the halo catalogues at all snapshots, separated by redshift intervals  $dz_i$ , as follows. Starting from each halo at  $z = 0$ , we define its progenitors at the previous output,  $z = dz_1$ , as all haloes containing at least one particle that at  $z = 0$  will belong to that halo. The 'main progenitor' at  $z = dz_1$  is defined as the progenitor that provided the largest mass contribution to the halo at  $z = 0$ . Next we repeat the same procedure, now starting at  $z = dz_1$  and considering progenitors at  $z = dz_1 + dz_2$ , and so on backward in time, always following the main progenitor halo. The resulting merger tree consists of a main trunk, which traces the main progenitor back in time, and of 'satellites', which are all the progenitors which, at any time, merge directly onto the main progenitor.

In the following analysis we only consider haloes at redshift  $z = 0$  whose main progenitor at any redshift has a virial mass  $M_v(z)$  not exceeding the final value  $M_v(z = 0) \equiv M_0$  by more than ten percent. In fact, any  $M_v(z)/M_0$  significantly larger than one corresponds to an incomplete merger in which two haloes first merge but subsequently split again. This typically occurs when a (relatively) small halo pass through a larger one. Since these events complicate our analysis, and their occurrence is only low, we decided to eliminate such merger histories.

For all simulations we split the halo samples at  $z = 0$  in mass bins of width  $d\log(M) = 0.5$ , with a minimum mass roughly corresponding to 200 particles within the virial radius for GIF and GIF2, and to 40000 particles for the resimulations. The actual mass bins for each run are listed in Table 1.

### 3 UNEVOLVED SUBHALO MASS FUNCTION

Starting from each halo at  $z = 0$ , we trace its merger history back in time and register all its satellites, i.e. all haloes directly accreted by the halo main progenitor at any output time. In order to remove subhaloes that at  $z = 0$  reside outside the host due to their elongated orbits (and so do not contribute to the subhalo population) we only consider satellites which donate at least 50% of their mass to the final halo. Let  $n(m_v/M_0, z)$  be the number of satellites of virial mass  $m_v$ , accreted at redshift  $z$  by a host halo with mass  $M_0$  at redshift zero. Integrating this expression over the redshift interval  $z_1 \leq z \leq z_2$ , we obtain the total number of satellites of mass  $m_v$  accreted by the main progenitor

during that interval,

$$N\left(\frac{m_v}{M_0}\right) = \int_{z_1}^{z_2} n\left(\frac{m_v}{M_0}, \zeta\right) d\zeta \quad (1)$$

which we term the *unevolved subhalo mass function*.

In Figure 2 we plot the unevolved subhalo mass function for different redshift intervals, as measured in the GIF (left) and GIF2 (right) simulations. The data points refer to different mass bins of the parent haloes at redshift  $z = 0$ , as indicated. As stated above, we only considered satellites that contributed at least 50% of their mass to the final ( $z = 0$ ) host. Setting  $z_1 = 0$  and  $z_2 = z_{\max}$ , which is the maximum redshift available in the simulations, we obtain the total, unevolved subhalo mass functions shown in the lower panels of Figure 2. Note that there is no indication for any significant dependence on  $M_0$ , indicating that the unevolved subhalo mass function is indeed universal, as found by van den Bosch et al. (2005). After some experimenting, we find that the unevolved subhalo mass function is well fitted by

$$\frac{dN}{d\ln(m_v/M_0)} = N_0 x^{-\alpha} e^{-6.283 x^3}, \quad x = \left| \frac{m_v}{\alpha M_0} \right| \quad (2)$$

with  $\alpha = 0.8$  and  $N_0 = 0.21$ . This fitting function is indicated by solid black lines in the lower panels.

In the upper and middle panels of Figure 2 we show the mass functions of the satellites accreted at redshifts larger and smaller than  $z_f$ , respectively. Here  $z_f$  is the so-called assembly redshift, defined as the *highest* redshift at which the mass of the main progenitor  $M_v(z)$  exceeds half the final value, (i.e.,  $M_v(z) > M_0/2$ ). Once again, the results for different host halo masses are indistinguishable, and are extremely well fit by equation (2) with  $\alpha = 0.8$ . The normalization,  $N_0$ , however, needs to be adjusted. Naively one would expect that both mass functions should have a normalization  $N_0/2$ . However, because of the discreteness of the merger histories, the average mass at the formation redshift,  $M(z_f)$ , is actually slightly larger than  $M_0/2$ . Sheth & Tormen (2004) have shown that, for the spherical collapse case and assuming a white noise power spectrum, the mass at formation has a distribution (eq.[4] of their paper) with a mean value  $\mu_{ST04}M_0 = (0.586 \pm 0.005)M_0$ . Here, combining haloes from GIF and GIF2, we find a mean formation mass  $\bar{\mu}_{GIF+GIF2}M_0 = (0.572 \pm 0.001)M_0$ . The fact that our results are somewhat lower owes to the fact that the distribution of  $\mu$  depends (weakly) on the power spectrum (see Sheth & Tormen 2004). The normalizations of the *unevolved subhalo mass function* accreted before  $N_{0,b}$  and after  $N_{0,a}$  the formation redshift are therefore:

$$N_{0,b} = \bar{\mu}N_0 = 0.572N_0, \quad (3)$$

$$N_{0,a} = (1 - \bar{\mu})N_0 = 0.428N_0. \quad (4)$$

These are the normalizations that we have adopted for the fitting functions shown in the upper and middle panels of Figure 2.

### 4 EVOLVED SUBHALO MASS FUNCTION

The evolved subhalo mass function at any redshift  $z$  is built from all the satellite haloes accreted by the main progenitor at all redshifts larger than  $z$ , where for each satellite we

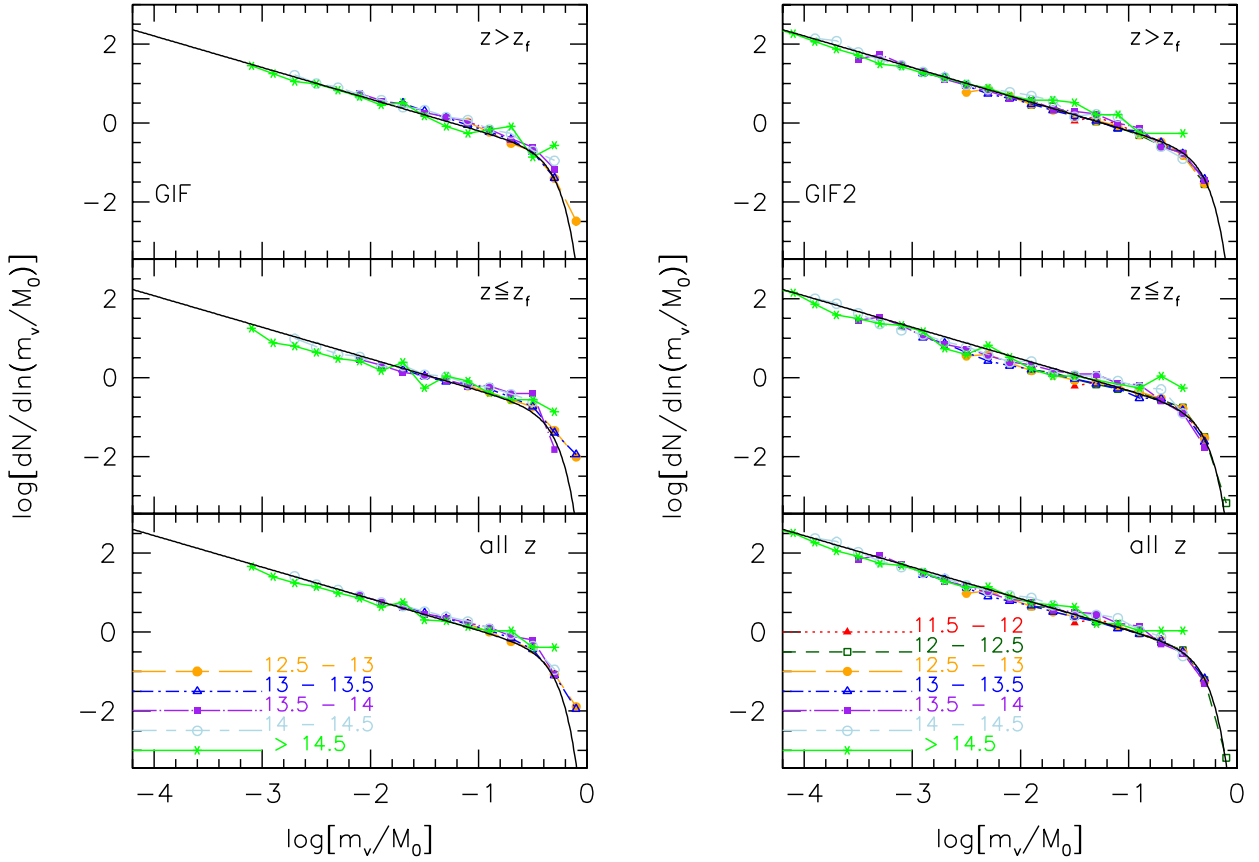


**Figure 2.** Mass functions of accreted satellites (unevolved subhalo mass functions). In the panels the various data points and line types refer to different present-day host halo masses. In the figures the the bounds of the mass bins are expressed in unit of  $\log(M_\odot/h)$ . The solid lines represent the fitting function to the distributions: equation (2) (see the main text for more details). Note that we only consider subhaloes that at  $z = 0$  contribute at least 50% of their mass. This ensures that at  $z = 0$  their center of mass lies within the virial radius of the host. *Top:* Unevolved subhalo mass function accreted before the formation redshift  $z_f$  of the host halo (defined as the earliest redshift when the mass of the main progenitor exceeds half the final mass). *Center:* Same as above, but only counting satellites accreted after  $z_f$ . *Bottom:* Same as above, but now counting satellites accreted at any redshift.

compute at each redshift its self-bound mass  $m_{sb}(z)$ . Operationally, we perform the following steps:

- given a satellite halo, we identify its merging redshift,  $z_m$ , defined as the latest redshift when the satellite was still an isolated halo, just before it was accreted by the main progenitor;
- we calculate the position of its center using the "moving center method" (Tormen et al. 1997), i.e. by repeated calculation of its center of mass using smaller and smaller radii to identify the subhalo densest core;
- we compute the subhalo tidal radius - as in Tormen et al (1998);
- we evaluate the binding energy of each subhalo particle by summing its potential energy (calculated using all particles inside the tidal radius) and its kinetic energy (using its residual velocity with respect to the average value inside the tidal radius);
- we remove all particles with positive binding energy, and iterate the previous steps until the self-bound subhalo mass converges.

With these data in hand, we can follow the time evolution of the self bound mass of each subhalo, snapshot by snapshot, from the merging redshift  $z_m$  to the present time  $z = 0$ . In the following Section we will use this information - gathered from the resimulated haloes - to estimate the subhalo mass-loss rates at all redshifts.

In Figure 3 we show a schematic representation of the merging history tree of a halo. Time runs upward, with the final halo depicted at the top. Light gray circles indicate the main progenitor at each time, whose history defines the 'main trunk' of the tree. Dark gray circles indicate satellite haloes, i.e. progenitor haloes accreted directly by the main trunk of the tree. The progenitors indicated by black circles are the 'leaves' of the merging-history tree, and reflect those progenitors whose mass is of the order of the resolution of the tree; i.e., for these haloes no progenitor can be identified in the simulation at earlier outputs. Satellites are either 'leaves', or they have progenitor haloes at earlier outputs, which in principle give rise to a population of sub-subhaloes, etc. In this paper we do not consider this substructure of subhaloes, though we intend to address their evolution in a forthcoming paper (Giocoli et al. in preparation).

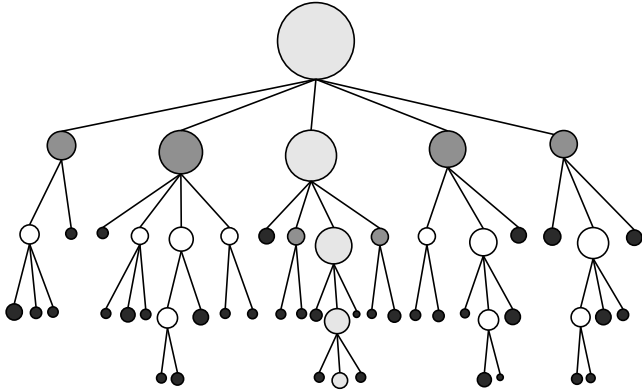


**Figure 3.** Schematic representation of the merging-history-tree of an halo. Solid light gray circles connected on the parent halo represent the main branch of the tree. Solid dark gray circles indicate satellites. Solid black circles indicate leaves progenitors. See the main text for explanation.

As an example, Figure 4 shows the subhalo population of the most massive halo found at  $z = 0$  in the GIF2 cosmological run. The left panel shows all particles inside the halo virial radius  $R_v$ . In the middle panel only those particles are shown that are bound to subhaloes located within  $R_v$ , while the right panel shows all other ‘field’ particles, which are bound to the main halo, but not to any subhalo.

In Figure 5 we plot the subhalo mass function for GIF2 haloes at redshift  $z = 0$ , split according to the final halo mass. We considered all self-bound subhaloes with at least 10 particles, and removed all subhaloes at halo-centric distances  $r < 0.05R_v$ , where the subhaloes are difficult to detect. Note that the evolved subhalo mass function is not universal, but depends on the mass of the final host halo, with more massive haloes hosting more subhaloes of a given  $m_{sb}/M_0$ .

The fact that the evolved subhalo mass function is not universal, but rather depends on host halo mass,  $M_0$ , was first shown by Gao et al. (2004). Using merger trees constructed with the extended Press-Schechter (EPS) formalism (e.g., Lacey & Cole 1993), and adopting a simple model for the average mass loss rate of subhaloes, van den Bosch et al. (2005) were able to reproduce these trends, which they explained in terms of (i) the universality of the unevolved subhalo mass function, and (ii) the fact that more massive haloes assemble later. The latter implies that smaller systems accrete their satellites at higher redshifts, when the haloes are denser, and the dynamical times are shorter. This, in turn, ensures that dynamical effects that promote mass loss are more efficient. Furthermore, satellites that are accreted earlier also are subjected to mass loss for a longer time. Both effects contribute to less massive host haloes having less substructure at  $z = 0$ .

Below we will show that the subhalo populations in our resimulated haloes agree well with this picture, and that indeed the average mass loss rates are higher at higher redshift. We will also find that the average mass loss rates are virtually independent of the mass ratio  $m_{sb}(z)/M_v(z)$  between the subhalo and its host.

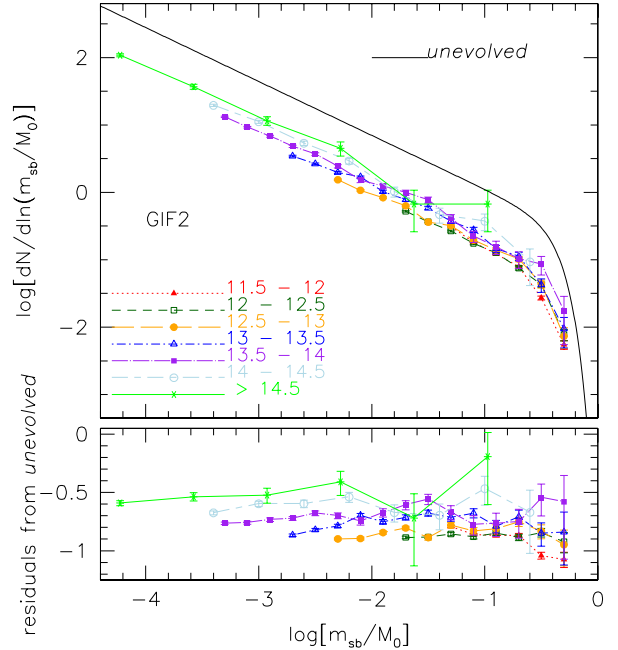


**Figure 5.** Subhaloes mass function of the self-bound particles of the haloes accreted by the main branch of the merger-history-tree of an halo, for GIF2 simulation. In the plot it has been considered all satellites with a distance from the center of the host halo less than the virial radius. We also plot the unevolved distribution: equation (2). The different data points and line types used are the same of Figure 2.

## 5 SUBHALO MASS LOSS RATES

In this section we estimate the subhalo mass loss rate, modeling it as a function of (i) the instantaneous satellite to host mass ratio:  $m_{sb}(z)/M_v(z)$ , (ii) the mass of the host halo at redshift zero:  $M_0$ , and (iii) the cosmic time through the redshift  $z$ . For this purpose we will use the subhalo population identified in the resimulations, as haloes in this sample have better force, mass and especially time resolution (88 snapshots between redshift ten and zero) than the cosmological GIF2 run. Since mass loss rates mostly depend on the local environment inside the host halo, the resimulated sample will provide correct rates even if the haloes themselves do not necessarily represent a fair sample for the given cosmological model.

In Figure 6 we show the unevolved subhalo mass function for satellites identified in the merger trees of the set of resimulated haloes; host haloes are split in three mass bins, according to Table 1. As for the GIF2 simulation, the unevolved subhalo mass function obtained from the resimulations is well fit by eq. 2.

After a satellite enters the virial radius of the host, various dynamical effects, including dynamical friction, tidal stripping, and close encounters with other subhaloes, cause the subhaloes to loose mass, and may eventually result in their complete disruption (e.g., Choi et al. 2007). The (average) mass loss rate of dark matter subhaloes is the direct link between the unevolved and evolved subhalo mass functions, and also is a fundamental ingredient for semi-analytical models of galaxy formation, as it sets the rate at which satellite galaxies merge with the central galaxy in



**Figure 4.** Subhalo population. Left: all particles composing the most massive halo found at  $z = 0$  in the GIF2 simulation; the virial mass for this halo is  $M_v = 1.8 \times 10^{15} M_\odot/h$ , resolved by more than one million particles. Center: particles bound to subhaloes at redshift  $z = 0$ . Right: particles bound to the main halo but not to subhaloes.

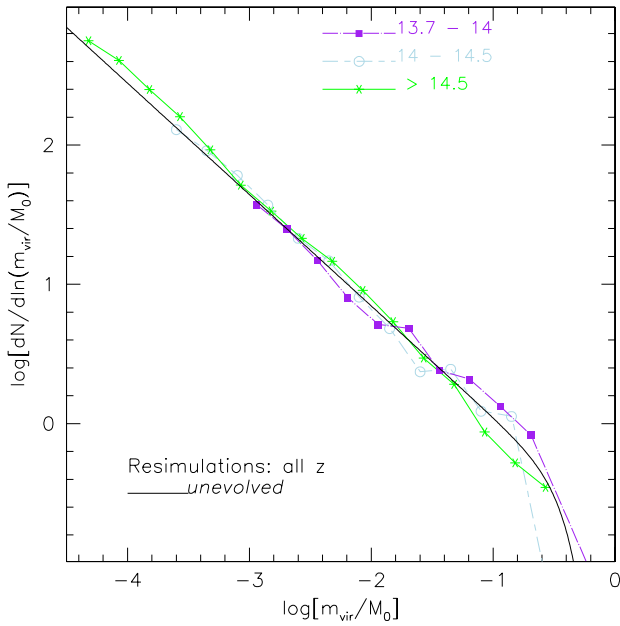


**Figure 6.** Unevolved subhalo mass function for the resimulated haloes. We notice that the function is independent of mass and well described by the same function fitting the GIF2 data (Figure 2). Haloes are split in three mass bins. In the figure the bounds of the bin are expressed in unit of  $\log(M_\odot/h)$ .

a halo, it determines the evolution of the mass-to-light ratios of satellite galaxies, and it regulates the importance of stellar streams in the haloes of central galaxies.

In this section we measure the mass loss rate experienced by each satellite. In addition, using statistical averaging, we determine the average mass loss rate of satellites as a function of the parameters listed at the beginning of this section. We define the average mass loss rate between two

successive snapshots at redshift,  $z_1$  and  $z_2$ , as

$$\frac{d}{dt} \left( \frac{m_{sb}}{M_v} \right) (z) = \frac{\frac{m_{sb}(z_2)}{M_v(z_2)} - \frac{m_{sb}(z_1)}{M_v(z_1)}}{t(z_2) - t(z_1)}, \quad z_1 < z < z_2. \quad (5)$$

where the values of  $m_{sb}(z)$  and  $M_v(z)$  are obtained by linear interpolation of the values at  $z_1$  and  $z_2$ . In Figure 7 we plot the subhalo mass loss rate as a function of the ratio  $m_{sb}(z)/M_v(z)$ ; Each panel refers to a different bin for the mass  $M_v(z)$  of the host halo.

The green points and band in each panel indicate the median and quartiles of the distribution. The thick magenta line represents a least squares fit to the median values in each panel; the fit is limited to the region where the median exhibits a linear behavior: we excluded by hand median values for  $m_{sb}/M_v$  close to one, which correspond to major mergers and cannot be described by a simple mass loss model. The thin dashed black line, identical in all panels, shows the global least square fit obtained using the data from all panels.

The data show a clear linear relation between  $m_{sb}/M_v$  and its time derivative, so we can write our model as:

$$\log \left| \frac{d(m_{sb}/M_v)}{dt} \right| = a \log(m_{sb}/M_v) + b. \quad (6)$$

Exponentiating this relation, and expanding the derivative on the LHS, we obtain:

$$\left| \frac{\dot{m}_{sb}}{M_v} - \frac{\dot{M}_v}{M_v} \frac{m_{sb}}{M_v} \right| = 10^b \left( \frac{m_{sb}}{M_v} \right)^a. \quad (7)$$

Due to the large number of snapshots in the resimulations, the time separation between two subsequent snapshots is always short:  $dt \approx 0.1$  Gyr. This is small enough to assume a constant mass for the host halo:  $\dot{M}_v = 0$ . By doing so, we obtain an expression for the *specific* mass loss rate

$$\frac{\dot{m}_{sb}}{m_{sb}} = -\frac{1}{\tau} \left( \frac{m_{sb}}{M_v} \right)^\zeta, \quad (8)$$

where the free parameters  $\tau(z, M_v) = 10^{-b}$  and  $\zeta(z, M_v) = a - 1$  might in principle depend both on cosmic time (or, equivalently, redshift  $z$ ) and on the virial mass  $M_v(z)$  of the

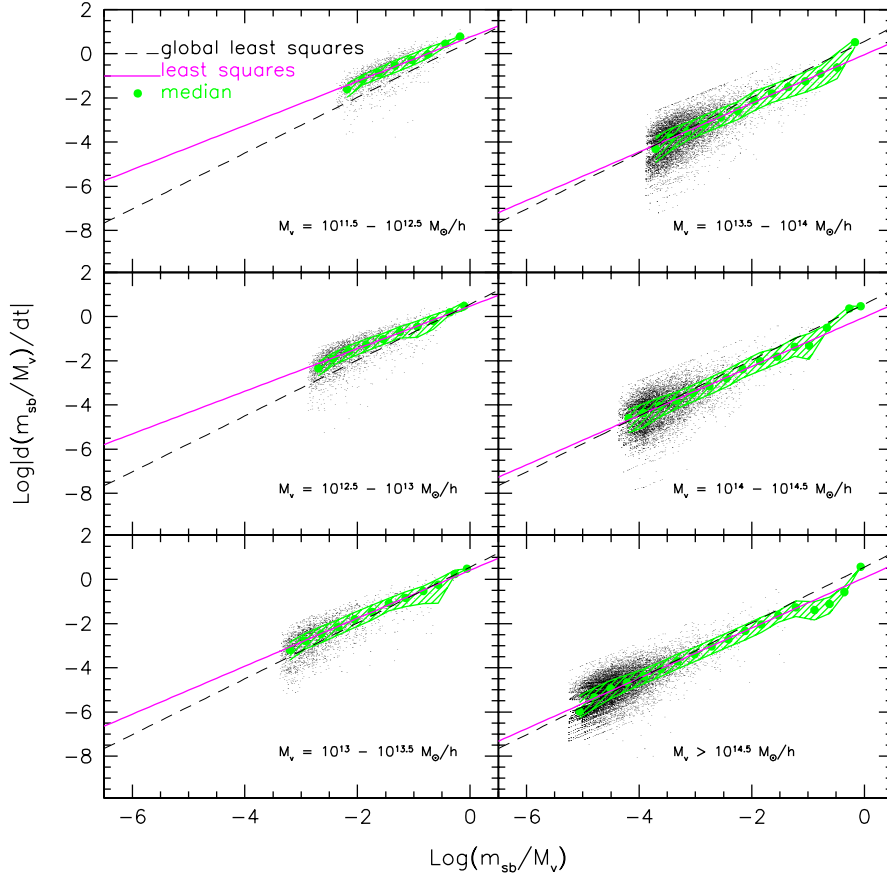


**Figure 7.** Subhalo mass loss rate. Each panel refers to a different bin in host halo virial mass at the redshift when the mass loss rate is computed. The filled circles represent the median of points and the hatched region the quartiles. The thick solid line is the least square fit to the median distribution for each panel. The thin dashed line is the average least squares for the different host halo masses.

host halo at that time. The negative sign arises from the mass loss of the satellites. Note that this specific mass loss rate is identical to that used by van den Bosch et al. (2005).

Figure 8 shows how the time scale of the mass loss rate,  $\tau = 10^{-b}$ , and  $\zeta = a - 1$ , as measured from the data shown in Figure 7, depend on the virial mass,  $M_v$ , of the instantaneous host halo. Error bars reflect the usual uncertainty on the coefficients obtained from the least square fitting. The slope is found to be independent of the mass of the host halo, with a best fit value of  $a = 1.07 \pm 0.03$  ( $\zeta = 0.07 \pm 0.03$ ). This implies that the specific mass loss rate is almost independent of the instantaneous mass ratio  $m_{sb}/M_v$ . On the other hand, the zero point,  $b$ , is found to be larger for less massive haloes.

In order to show the typical spread of points in each panel of Fig. 7 around each median, in the bottom panel of Figure 8 we show the average (over the six panels of Figure 7) of the differences between each quartile and the median itself. We see that on average fifty percent of the points lay roughly within a distance  $\log y = \pm 0.3$  from the median; that is, typical mass losses deviate from their median value by less than a factor of two.

In Figure 9 we plot the subhalo mass loss rate versus the ratio  $m_{sb}(z)/M_v(z)$ , now binned according to the redshift

at which the mass loss rate is calculated. Medians, quartiles and lines are as in Figure 7. The time scale  $\tau$  and  $\zeta$  for the six panels are shown in Figure 10, plotted versus the mean redshift of each of the six bins; in the bottom panel the average quartile distribution for each fit (as explained above) is shown. The red solid curve superimposed to the trend in zero point is the equation

$$\tau(z) = \tau_0 \left[ \frac{\Delta_v(z)}{\Delta_0} \right]^{-1/2} \left[ \frac{H(z)}{H_0} \right]^{-1}, \quad (9)$$

with  $H(z)$  the Hubble constant at redshift  $z$ , and with  $\tau_0 = 2.0$  Gyr.

This equation was proposed by van den Bosch et al. (2005) and describes the redshift dependence of mass loss rates obtained under the assumption that  $\tau$  is proportional to the dynamical time  $t_{dyn} \propto \rho_v^{-1/2}(z)$ , taking into account that, according to the spherical collapse model, the average density within the virial radius,  $\rho_v$  is independent of halo mass at fixed redshift. This means that we can write  $\tau(M_v, z) = \tau(z)$ . The red line in Figure 10 shows that indeed this provides a good description of the measured mass loss rates.

Note, though, that Figure 8 suggests that the average mass loss rates also depend on host halo mass. In order to reconcile this with the claim that the zero-point is indepen-

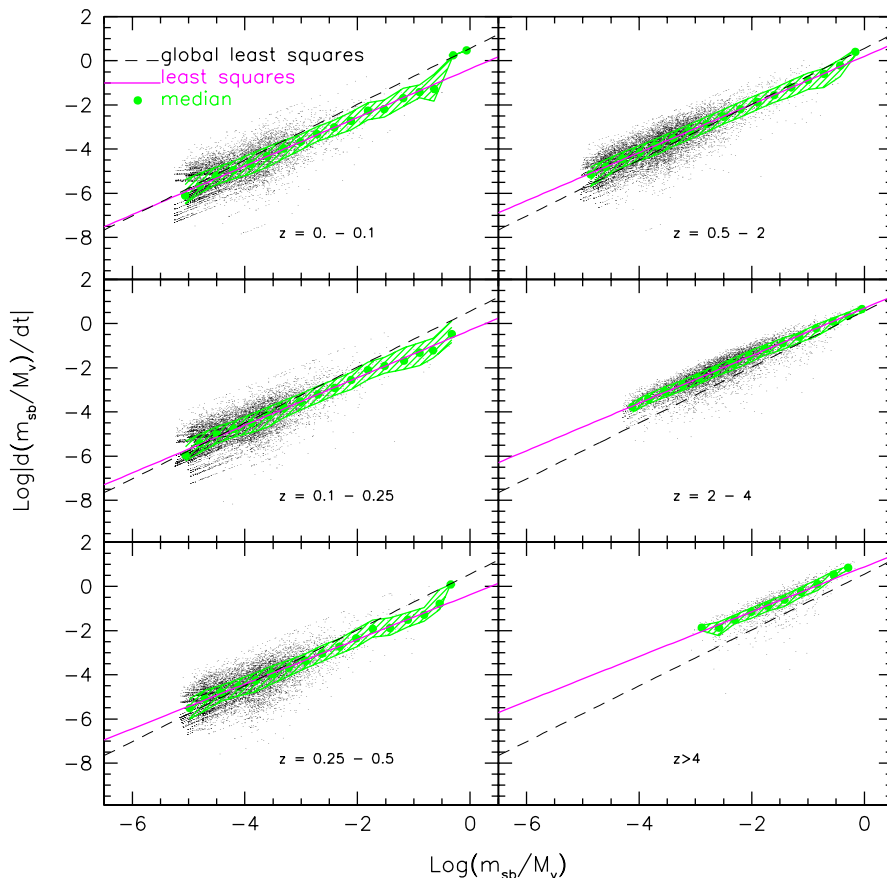


**Figure 9.** Subhalo mass loss rate. Each panel refers to a different bin in the redshift at which the mass loss rate is computed. Symbols and lines are as in Figure 7.

dent of  $M_v$ , recall that, on average, more massive haloes assemble (and thus accrete their satellites) earlier than less massive haloes. Therefore, the different panels of Figure 7 actually refer to different average redshifts, with larger  $M_v$  corresponding to a lower average redshift. Consequently, the ‘apparent’ mass dependence evident in the upper panel of Figure 8 is merely a reflection of the redshift dependence described by equation (9). To demonstrate this we now split the data points of each panel of Figure 9 in different subsets, according to the mass of the host halo. Figure 11 shows the average slopes and zero points obtained for these subsets using least-squares fitting. This clearly shows that the characteristic time scale for mass loss (given by the zero point) is independent of the host mass  $M_v(z)$  at fixed redshift, in accord with equation (9).

Thus, to good approximation, the average mass loss rate of dark matter subhaloes depends only on the density of the host halo, and thus on redshift (or cosmic time), but not on the mass of the host halo. Furthermore, since the best-fit value of  $\zeta$  is close to zero, to good approximation subhalo masses decay exponentially<sup>1</sup> according to

$$m_{sb}(t) = m_v \exp \left[ -\frac{t - t_m}{\tau(z)} \right], \quad (10)$$

<sup>1</sup> this follows from a simple integration of equation (8) with  $\zeta = 0$

where  $m_v$  is the mass of the satellite at the time of accretion,  $t_m$ , and  $\tau(z)$  is given by equation (9) with  $\tau_0 = 2.0$  Gyr.

## 6 MONTE CARLO SIMULATION

In this section we compare our results to those of van den Bosch et al. (2005), and we use their Monte Carlo method to check the self-consistency of the results presented above, i.e., we check whether the (universal) unevolved subhalo mass function, combined with the satellite accretion times and the average mass loss rates, can reproduce the evolved subhalo mass functions presented in Section 4.

The Monte-Carlo method of van den Bosch et al. (2005) starts by constructing EPS merger trees using the method described in van den Bosch (2002) (see also Somerville & Kolatt 1999). These merger trees are then used to register the accretion times and masses of satellites merging onto the main progenitor. Starting from these inputs, van den Bosch et al. (2005) then proceeded as follows. In between two time-steps, they evolve the masses of the subhaloes using equations 8 and 9. The two free parameters,  $\tau_0$  and  $\zeta$  were tuned to reproduce the subhalo mass function of massive, cluster sized haloes obtained from numerical simulations by Gao et al. (2004), De Lucia et al. (2004) and Tormen et al. (2004). This resulted in  $\tau_0 = 0.13$

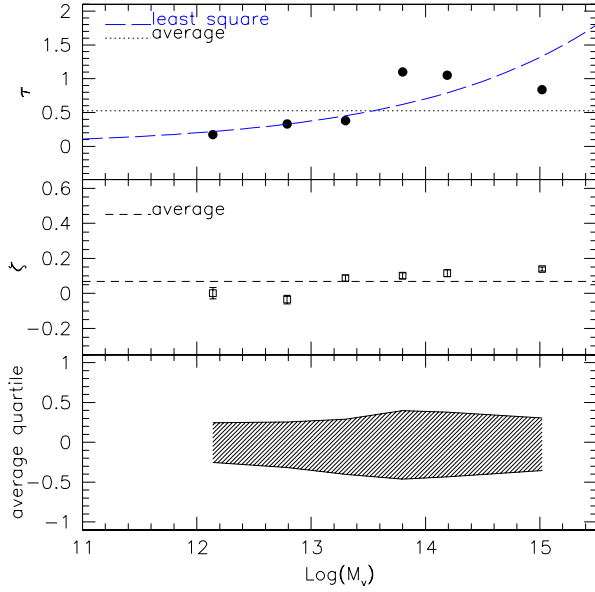


**Figure 8.** Dependence of the fit parameters of the Figure 7 on the host halo virial mass. The top panel shows the time scale of the mass loss rate  $\tau = 10^{-b}$ . The average and the least square fit of the data points have been computed on the plane  $(b, M_v)$ . In the central panel we show the dependence of parameter  $\zeta = a - 1$  on  $M_v$ . In the bottom panel we show the spread of the first and third quartiles around the median, averaged over the six panels of Figure 7 (see the main text for a detailed explanation).

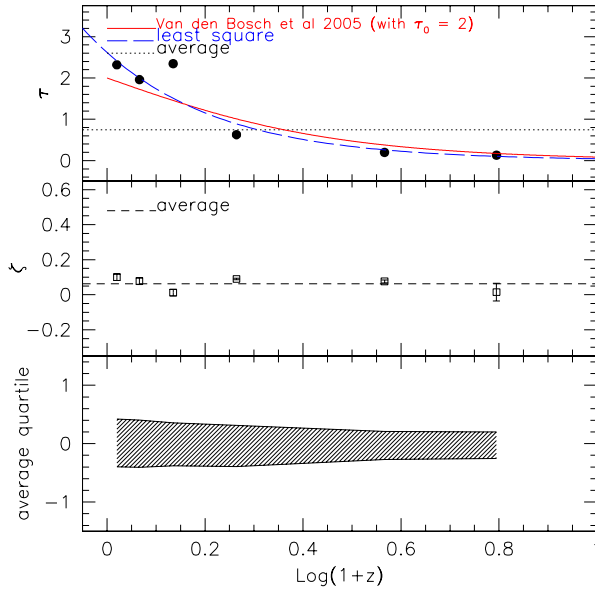


**Figure 10.** Time scale of the mass loss rate and  $\zeta$  in terms of the redshift at which the subhaloes are experiencing mass loss (Figure 9). The average and the least squares fit of the top panel were computed on the plane  $(b, z)$ . The bottom panel shows the average first and third quartile for the median distribution in each panel of the Figure 9, constructed as previously described in the main text.

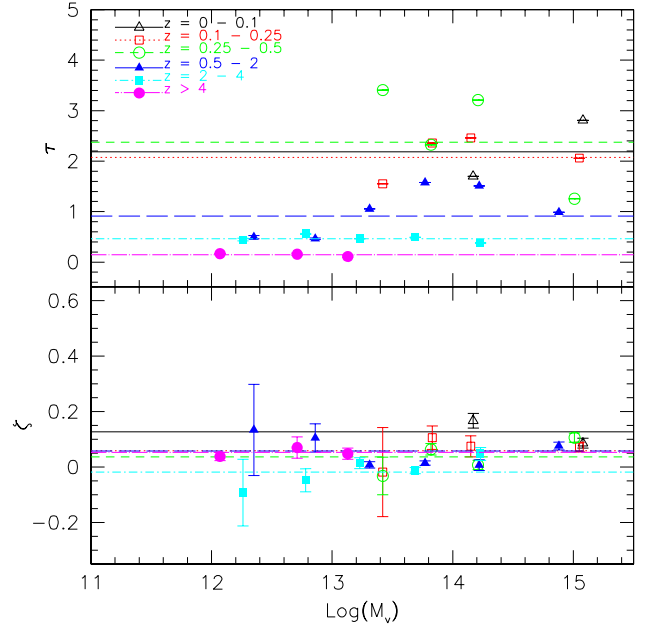


**Figure 11.** Time scale of the mass loss rate and  $\zeta$  versus host mass, for six fixed redshift bins – represented by different data points. The horizontal lines, with various line type, show the average  $b = -\log(\tau)$  and  $\zeta$  for each redshift bin.

Gyr and  $\zeta = 0.36$ , which differs substantially from the results obtained here:  $\tau_0 = 2.0$  Gyr and  $\zeta = 0.06$ . The reason for this discrepancy owes to the use of EPS merger trees, as opposed to merger trees extracted from numerical simulations. In fact, the unevolved subhalo mass function obtained by van den Bosch et al. (2005) differs significantly from that shown in Figures 2 and 6, in that it is significantly higher, and with a different slope at the low mass end<sup>2</sup>. Consequently, in order to reproduce the subhalo mass functions obtained from numerical simulations, van den Bosch et al. (2005) had to adopt higher mass loss rates (i.e., a lower value for  $\tau_0$ , and a different mass dependence (i.e., a different value for  $\zeta$ ).

The fact that EPS merger trees predict an unevolved subhalo mass function that differs significantly from that obtained in numerical simulations, should not come entirely as a surprise. After all, the construction of EPS merger trees relies on the spherical collapse model (see Lacey & Cole 1993; Somerville & Kolatt 1999). However, in reality, the collapse of dark matter haloes is influenced by the surrounding tidal force field, making the collapse ellipsoidal, rather than spherical (e.g., Sheth & Tormen 1999; Sheth, Mo & Tormen 2001; Sheth & Tormen 2002). As shown by Sheth & Tormen (2002), the conditional and unconditional mass functions are different under ellipsoidal collapse conditions than under spherical collapse conditions, which has important consequences for the accuracy of the EPS merger trees. For instance, the halo formation times predicted by EPS are systematically offset from those

<sup>2</sup> It is noteworthy, though, that the EPS formalism predicts that the unevolved subhalo mass function is universal, i.e., independent of the host mass, in good agreement with the simulation results presented here.

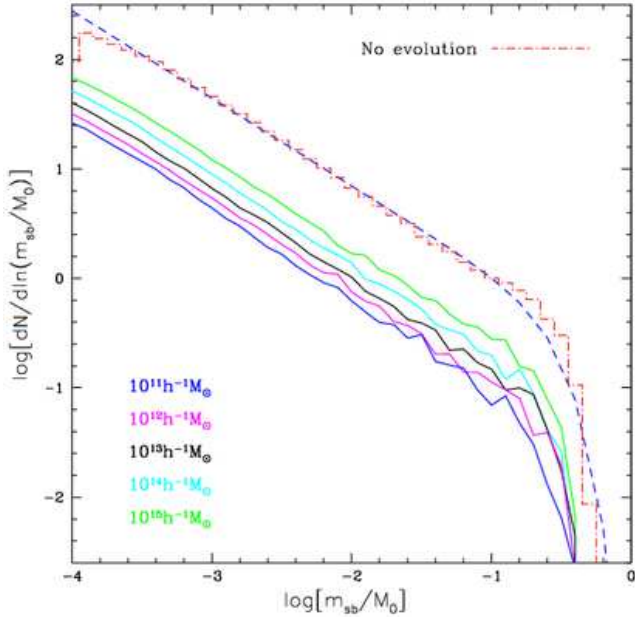


**Figure 12.** The dotted histogram shows the mass accreted by the main branch in the Monte Carlo merger tree with the overplotted equation (2). The solid lines represent the subhaloes mass function obtained evolving the mass accreted by the main progenitors of different present day  $M_0$ -halo.

obtained from numerical simulations (Lacey & Cole 1993; Somerville et al. 2000; van den Bosch 2002; Wechsler et al. 2002; Giocoli et al. 2007), while the average mass of the main progenitor is typically overestimated (Somerville et al. 2000).

To perform the self-consistency check mentioned above, we therefore use the same Monte-Carlo method as van den Bosch et al. (2005), but we randomly remove satellite-branches from the merger tree with a probability

$$P_{\text{reject}} = \frac{n_{\text{sim}}(m_v/M_0)}{n_{\text{EPS}}(m_v/M_0)} \quad (11)$$

where  $n_{\text{sim}}$  and  $n_{\text{EPS}}$  are the unevolved subhalo mass functions obtained from the simulations and from the EPS merger trees, respectively. This ensures that the Monte Carlo method uses an effective, unevolved subhalo mass function that is identical to that of equation (2).

As in van den Bosch et al. (2005) we evolve the masses of the subhaloes using equations 8 and 9 with  $\tau_0 = 2.0$  Gyr and  $\zeta = 0.06$ , which are the best-fit values obtained in section 5. The resulting evolved subhalo mass functions, for five different masses of the present-day host halo, are shown in Figure 12, together with the unevolved subhalo mass function obtained using the rejection scheme outlined above (and which is independent of the host halo mass). Each evolved subhalo mass function is the average obtained from 2000 merger tree realizations (see van den Bosch et al. 2005, for details). A comparison with the evolved subhalo mass functions obtained from our numerical simulations, and shown in Figure 12, shows good agreement. This indicates that the evolved subhalo mass functions are self-consistent with the (universal) unevolved subhalo mass function and the simple form for the average mass loss rate obtained in this paper.

## 7 SUMMARY AND CONCLUSIONS

In this paper we have studied the mass loss rate of dark matter subhaloes using a set of high resolution  $N$ -body simulation of structure formation. Haloes were followed backward in time along the main branch of their merging history tree. At each snapshot the satellites accreted by the main branch were identified. We showed that the mass function of accreted satellites (unevolved subhalo mass function) is universal, that is, it does not depend on the present day host halo mass  $M_0$ , and we presented a fitting function for this distribution.

We then followed each accreted satellite forward in time, snapshot by snapshot, computing its self-bound mass and its mass loss rate. We found that the expression for the mass loss rate proposed by van den Bosch et al. (2005) is consistent with  $N$ -body simulations, and excellent agreement is obtained if the value with  $\tau_0 = 2.0$  Gyr is taken. In addition, we find that the average mass loss rate is virtually independent of the instantaneous mass ratio  $m_{\text{sb}}/M_v$  between the subhalo and its host halo. This differs substantially from the best-fit mass loss rate parameters obtained by van den Bosch et al. (2005) using EPS merger trees. In particular, van den Bosch et al. (2005) obtained  $\tau_0 = 0.13$  Gyr, and a significant dependence on  $m_{\text{sb}}/M_v$ . The reason for this discrepancy is that the unevolved subhalo mass function of EPS merger trees is too high, so that a higher mass loss rate was inferred to be consistent with the evolved subhalo mass functions in numerical simulations.

With an unevolved subhalo mass function that is universal, and an average mass loss rate that is virtually independent of  $m_{\text{sb}}/M_v$ , it becomes straightforward to understand why less massive haloes have evolved subhalo mass functions with a lower normalization. This simply owes to the fact that less massive haloes assemble earlier, which implies that they accrete their satellites earlier. At earlier times the mass loss rate is higher, because the dynamical times of dark matter haloes are shorter. In addition, a subhalo that is accreted earlier is subjected to mass loss for a longer period. Both these effects contribute to the fact that less massive haloes have less substructure.

The present description does not consider the possible presence of subhaloes within subhaloes, accreted along the tree of each present day subhalo. In a follow-up paper (Giocoli et al. 2008, in preparation) we will investigate this issue in detail, comparing the populations of subhaloes found using different techniques.

## 8 ACKNOWLEDGMENTS

This work has been partially supported by Italian PRIN and ASI.

Thanks to Ravi K. Sheth, Robert Smith and Gao Liang for useful discussions and comments. Thanks also to Marco Comparato and Ugo Becciani for useful assistance with VisIVO (Comparato et al. 2007): a visualization interface for numerical simulation.

## REFERENCES

- Benson A.J., Lacey C.G., Baugh C.M., Cole S., Frenk C.S., 2002, MNRAS, 333, 156
- Benson A.J., Lacey C.G., Frenk C.S., Baugh C.M., Cole S., 2004, MNRAS, 351, 1215
- Bertone, G. 2006, Physical Review D, 73, 103519
- Bullock, J. S., Kravtsov, A. V., & Weinberg, D. H. 2000, ApJ, 539, 517
- Choi, J.-H., Weinberg, M. D., & Katz, N. 2007, MNRAS, 381, 987
- Comparato, M., Becciani, U., Costa, A., Larsson, B., Garilli, B., Gheller, C., & Taylor, J. 2007, The Publications of the Astronomical Society of the Pacific, 119, 898
- Dalal N., Kochanek C.S., 2002, ApJ, 572, 25
- De Lucia, G., et al. 2004, MNRAS, 348, 333
- Diemand, J., Kuhlen, M., & Madau, P. 2007, ApJ, 657, 262
- Dolag, K., Vazza, F., Brunetti, G., & Tormen, G. 2005, MNRAS, 364, 753
- Eke, V. R., Cole, S., & Frenk, C. S. 1996, MNRAS, 282, 263
- Gao, L., White, S. D. M., Jenkins, A., Stoehr, F., & Springel, V. 2004, MNRAS, 355, 819
- Giocoli, C., Moreno, J., Sheth, R. K., & Tormen, G. 2007, MNRAS, 111
- Goerdt T., Gnedin O.Y., Moore B., Diemand J., Stadel J., 2007, MNRAS, 375, 191
- Kamionkowski, M., & Liddle, A. R. 2000, Physical Review Letters, 84, 4525
- Kauffmann, G., Colberg, J. M., Diaferio, A., & White, S. D. M. 1999, MNRAS, 303, 188
- Koushiappas S., 2006, Phys. Rev. Letter, 97, 1301
- Kravtsov, A. V., Gnedin, O. Y., & Klypin, A. A. 2004a, ApJ, 609, 482
- Kravtsov, A. V., Berlind A.A., Wechsler R.H., Klypin, A.A., Gottlöber S., Allgood B., Primack J.R., 2004b, ApJ, 609, 35
- Lacey, C., & Cole, S. 1993, MNRAS, 262, 627
- Metcalf R.B., Madau P., 2001, ApJ, 495, 139
- Moore, B., Ghigna, S., Governato, F., Lake, G., Quinn, T., Stadel, J., & Tozzi, P. 1999, ApJ, 524, L19
- Pieri, L., Bertone, G., & Branchini, E 2007, ArXiv e-prints, 706, arXiv:0706.2101
- Seljak, U., & Zaldarriaga, M. 1996, ApJ, 469, 437
- Sheth, R. K., & Tormen, G. 1999, MNRAS, 308, 119
- Sheth, R. K., Mo, H. J., & Tormen, G. 2001, MNRAS, 323, 1
- Sheth, R. K., & Tormen, G. 2002, MNRAS, 329, 61
- Sheth, R. K., & Tormen, G. 2004, MNRAS, 349, 1464
- Somerville, R. S., & Kolatt, T. S. 1999, MNRAS, 305, 1
- Somerville, R. S., Lemson G., Kolatt T. S., & Dekel A., 2000, MNRAS, 305, 1
- Somerville, R. S. 2002, ApJl, 572, L23
- Springel, V. 2005, MNRAS, 364, 1105
- Steward K.R., Bullock J.S., Wechsler R.H., Maller A.H., Zentner A.R., 2007, preprint (arXiv:0711.5027)
- Stoehr, F., White, S. D. M., Springel, V., Tormen, G., & Yoshida, N. 2003, MNRAS, 345, 1313
- Stoehr, F., White, S. D. M., Tormen, G., & Springel, V. 2002, MNRAS, 335, L84
- Taylor J.E., Babul A., 2004, MNRAS, 348, 811
- Tormen, G., Bouchet, F. R., & White, S. D. M. 1997, MNRAS, 286, 865
- Tormen, G., Diaferio, A., & Syer, D. 1998, MNRAS, 299, 728
- Tormen, G., Moscardini, L., & Yoshida, N. 2004, MNRAS, 350, 1397
- Tóth G., Ostriker J.P., 1992, ApJ, 389, 5
- Vale A., Ostriker J.P., 2006, MNRAS, 371, 1173
- van den Bosch, F. C. 2002, MNRAS, 331, 98
- van den Bosch, F. C., Tormen, G., & Giocoli, C. 2005, MNRAS, 359, 1029
- Yoshida, N., Sheth, R. K., & Diaferio, A. 2001, MNRAS, 328, 669
- Wechsler, R. H., Bullock, J. S., Primack, J. R., Kravtsov, A. V., & Dekel, A. 2002, ApJ, 568, 52
- White, S. D. M., & Rees, M. J. 1978, MNRAS, 183, 341
- Zentner A.R., Bullock J.S., 2003, ApJ, 598, 49